Human organoid model of PCH2a recapitulates brain region-specific pathology

Theresa Kagermeier 1,2, Stefan Hauser 1,3, Kseniia Sarieva 1,2,4, Lucia Laugwitz 5, Samuel Groeschel 5, Wibke Janzarik 6, Zeynep Yentür 1, 2, 4, 7, Katharina Becker 1, Ludger Schöls 1,3, Ingeborg Krägeloh-Mann 5, Simone Mayer 1,7*

1 Hertie Institute for Clinical Brain Research, University of Tübingen, Tübingen, Germany
2 Graduate Training Centre of Neuroscience, University of Tübingen, Tübingen, Germany
3 German Center for Neurodegenerative Diseases, Tübingen, Germany
4 International Max Planck Research School, Graduate Training Centre of Neuroscience, University of Tübingen, Tübingen, Germany
5 Department of Neuropediatrics, Developmental Neurology and Social Pediatrics, University of Tübingen
6 Department of Neuropediatrics and Muscle Disorders, Center for Pediatrics and Adolescent Medicine, Medical Center, Faculty of Medicine, University of Freiburg, Freiburg, Germany
7 Heidelberger Akademie der Wissenschaften, Heidelberg, Germany.

*Corresponding author:

Dr. Simone Mayer
Hertie Institute for Clinical Brain Research
Otfried-Müller Str. 25
72076 Tübingen, Germany
Email: si.mayer@uni-tuebingen.de
Phone: +49 (0)7071 29-88870

Abstract

Pontocerebellar hypoplasia type 2 a (PCH2a) is a rare, autosomal recessive neurogenetic disorder. Affected individuals present with early and severe neurological impairment. The anatomical hallmark of PCH2a is the hypoplasia of the cerebellum and pons accompanied by progressive microcephaly over the first years of life (OMIM #277470). Treatment options are limited and symptomatic. PCH2a results from a homozygous founder variant in the *TSEN54* gene (OMIM *608755), which encodes a tRNA splicing endonuclease complex subunit. A recent study revealed altered tRNA pools in fibroblasts from affected individuals with PCH2a. However, the pathological mechanism underlying the hypoplasia of the cerebellum and the progressive microcephaly is unknown due to a lack of a model system. Leveraging recent progress in organoid generation, we developed human models of PCH2a using brain region-specific organoids. We, therefore, obtained skin biopsies from three affected males with genetically confirmed PCH2a and derived induced pluripotent stem cells (iPSCs). Cerebellar and neocortical organoids were differentiated from control and affected iPSCs and showed expression of TSEN54. In line with neuroimaging findings in affected individuals, PCH2a cerebellar organoids are reduced in size compared

to controls starting early in differentiation. While neocortical PCH2a organoids also show growth deficits, they are less pronounced than those in cerebellar organoids, reminiscent of the progressive microcephaly in PCH2a. In addition, we do not find evidence of increased apoptosis in PCH2a organoids compared to controls in contrast to what has been suggested in loss-of-function animal models. We have generated a human model of PCH2a, which will allow to decipher disease mechanisms in depth in order to explain how a variant in a ubiquitously expressed gene involved in tRNA metabolism causes pathology in specific brain regions.

Introduction

Pontocerebellar hypoplasias (PCH) comprise a heterogeneous group of neurogenetic disorders characterized by a severe neurodevelopmental impairment and hypoplasia of the cerebellum and pons (Figure 1A,B) (van Dijk et al., 2018). Besides the primary pontocerebellar hypoplasia, affected individuals develop progressive microcephaly (Barth et al., 2007; Namavar et al., 2011a). PCH2 is the most common PCH but is still ultra-rare (1:100,000 births) (Budde et al., 2008; Sanchez-Albisua et al., 2014). Clinically, PCH2 is characterized by profound neurodevelopmental delay, causing a significant burden to affected individuals and their families (Ammann-Schnell et al., 2021; Sanchez-Albisua et al., 2014). To date, no curative treatment is available, and disease management is focused on alleviating symptoms.

90% of PCH2 cases are caused by a homozygous founder variant in the *TSEN54* gene (NM_207346.3:c.919G>T, p.(Ala307Ser)) and are referred to as PCH2a (Budde et al., 2008; van Dijk et al., 2018). *TSEN54* encodes a subunit of the tRNA splicing endonuclease (TSEN) complex, which is required to remove introns from pre-tRNAs (Trotta et al., 2006). A subset of tRNAs requires splicing before providing amino acids to the ribosome during translation (Chan and Lowe, 2009). The variant is in an unstructured region of the protein, not near the active site (Hayne et al., 2022; Sekulovski et al., 2021). While bi-allelic pathogenic variants in *TSEN54* do not affect the endonuclease activity of the TSEN complex in fibroblasts of affected individuals (Budde et al., 2008; Sekulovski et al., 2021), they result in a destabilization of the complex and altered tRNA pools (Sekulovski et al., 2021). The TSEN54 protein is expressed throughout the body at varying levels (Human Protein Atlas)(Uhlen et al., 2015). At the mRNA level, *TSEN54* is widely expressed in the developing human brain (Human Brain Transcriptome)(Kang et al., 2011) starting in the first trimester of gestation (Kasher et al., 2011). In the second trimester of gestation, *TSEN54* is expressed highly in the developing cerebellum, pons, and olivary nuclei (Budde et al., 2008). Its expression does not seem cell type-specific in the developing neocortex and cerebellum at the level of mRNA (Aldinger et al., 2021; Nowakowski et al., 2017). It is unclear why specifically cerebellum and pons are affected in PCH2a (Kasher et al., 2011). Variants in genes responsible for tRNA metabolism cause several neurodevelopmental disorders (Schaffer et al., 2019). Therefore it has been hypothesized that specific brain areas are especially vulnerable to TSEN malfunction due to a specific requirement of this complex during early postnatal development (Budde et al., 2008).

Efforts to establish the cellular mechanism of pathophysiology in animal models have been inconclusive so far. While the TSEN complex is conserved from archaea, *TSEN54* has undergone evolutionary changes in the primate lineage (Lee et al., 2016b). Notably, the amino acid sequence around *TSEN54* :c.919G>T, p.(A307S) is not conserved between species (Budde et al., 2008). Of the frequently used model organisms, only mouse and chicken share the amino acid residue (Budde et al., 2008). A recently developed fly model

of PCH shows defects in brain development, death at larval stages, and apoptosis upon loss of function of the *TSEN54* ortholog, but the relevance to the brain region-specific clinical phenotype is unclear (Schmidt et al., 2022). In zebrafish, loss of *tsen54* function leads to cell death in the brain during development (Kasher et al., 2011). A complete loss of Tsen54 in mice results in early embryonic lethality (Ermakova et al., 2018). Moreover, bi-allelic variants of *TSEN54* in dogs lead to a neurological disorder characterized by leukodystrophy, a disease with strikingly different pathophysiology (Stork et al., 2019). These findings imply a potential species-specific effect of TSEN54 malfunction on brain development. Additionally, the brain has changed tremendously in evolution, especially in the primate lineage (Herculano-Houzel, 2012). Compared to mouse, the human neocortex has expanded dramatically (1000x in the number of neurons and surface area), has a protracted development (neurogenesis is 20x longer than in mouse) and displays an unprecedented cellular heterogeneity (Geschwind and Rakic, 2013; Miller et al., 2019). Similarly, the human cerebellum has a 750-fold greater surface area than the mouse, a protracted development occurring over 2-3 years compared to 30-35 days, and additional transient structures (Haldipur et al., 2022). Taken together, the lack of appropriate models of PCH2a has to date precluded the elucidation of its molecular pathology.

In this study, we leverage the recent developments in the generation of brain region-specific organoids (Zhang et al., 2022) to create a human model of PCH2a. We identified three individuals that display the genetic, clinical and brain imaging features previously described for PCH2a and derived induced pluripotent stem cells (iPSCs) from fibroblasts. We differentiated PCH2a and control iPSC towards a cerebellar and neocortical fate in organoid cultures and showed that they express TSEN54 at the RNA and protein levels and may thus serve as an appropriate model for PCH2a. Growth curves of organoids recapitulated the brain region-specific pathology observed in affected individuals. Cerebellar PCH2a organoids were severely reduced in size compared to controls, while neocortical PCH2a organoids showed less severe divergence from controls only at later stages of differentiation. We did not find any difference in the induction of apoptosis, indicating that size differences are likely explained by altered proliferation and differentiation in PCH2a organoids at these early stages of development.

Results

Generation of PCH2a-derived iPSCs

It is unclear how a ubiquitously expressed gene involved in tRNA metabolism causes pathology only in specific tissues and even within the nervous system, with differential pathology in different brain regions. Based on recent successes in modeling neurogenetic disorders in organoids (Khakipoor et al., 2020; Velasco et al., 2020), we reasoned that a human iPSC-based brain organoid model could recapitulate pathological hallmarks of PCH2a. To our knowledge, cerebellar organoids have not yet been used to model neurogenetic disorders involving the cerebellum. We therefore hypothesized that generating neocortical and cerebellar organoids might model the brain region-specific pathology in PCH2a.

As a first step, we identified three affected males with genetically confirmed PCH2a, harboring the c.919G>T variant in the *TSEN54* gene in the homozygous state. Clinical features typical of PCH2a were evident in all probands (Sanchez-Albisua et al., 2014). In summary, subjects displayed severe developmental delay with minimal cognitive and motor development, seizures of variable semiology, and a severe dystonic movement disorder. Moreover, the probands exhibited neurogenic dysphagia and gastrointestinal disturbances. Neuroimaging revealed severe hypoplasia of the brainstem, pons and

cerebellum in contrast to less severe volume reduction of the cerebrum (Figure 1A, B illustrates this in one affected child (donor of iPSC line PCH-02) in comparison to an age-matched control).

We obtained skin biopsies from the three probands, extracted fibroblasts and derived iPSCs using an episomal reprogramming approach (Figure 1C) (Okita et al., 2013). iPSCs were subjected to a range of quality controls. First, we stained cells for alkaline phosphatase (ALP), a marker of pluripotency (Figure 1D). Next, we confirmed pluripotency using immunocytochemistry for OCT4 and TRA1-81 (Figure 1E,F) and qRT-PCR for *OCT3/4, SOX2, KLF4, cMYC, NANOG and DNMT3B* (Supplementary Figure 1A). Pluripotency was further corroborated using spontaneous tri-lineage differentiation (Korneck et al., 2022). iPSCs differentiated into the three primordial germ layers, namely, ectoderm (Tuj1), mesoderm (SMA), and endoderm (FOXA2) (Figure 1G-I). Sanger sequencing confirmed the presence of the disease-causing variant in all iPSC lines (Supplementary Figure 1B). SNP array analysis revealed no genomic aberrations induced by the reprogramming. Control lines used in this study were generated following the same protocol and were subjected to all aforementioned quality controls. Moreover, immunocytochemistry against TSEN54 demonstrated that all PCH2a iPSC lines expressed TSEN54 (Figure 1J).

TSEN54 expression in cerebellar and neocortical organoids

To model brain region-specific pathology, we then differentiated three control and the PCH2a iPSCs lines towards a cerebellar and neocortical fate in 3D using established protocols (Pasca et al., 2015; Silva et al., 2020) (Figure 2A). We aimed to test if cerebellar organoids recapitulated the expression of *TSEN54* observed in primary tissue during the first and second trimesters of gestation (Budde et al., 2008; Kasher et al., 2011). We analyzed the expression of *TSEN54* at the RNA level using qRT-PCR. *TSEN54* was expressed in iPSCs and D20 cerebellar and neocortical organoids with no significant difference in expression levels. Further, there was no significant difference between PCH2a and control samples. (Figure 2B). Immunohistochemistry against TSEN54 confirmed expression at D50 of differentiation in PCH2a and control cerebellar and neocortical organoids (Figure 2 C-F). Taken together, both cerebellar and neocortical organoids expressed TSEN54 making them a suitable human disease model to study PCH subtypes caused by variants in TSEN54, including PCH2a. In line with the “housekeeping” function of TSEN54, we did not find differences in expression between cell and tissue types.

Human brain organoids have brain region-specific growth deficits

We next determined if cerebellar hypoplasia and progressive microcephaly found in affected individuals (Figure 1A,B) were recapitulated in our *in vitro* model (Figure 2A). We, therefore, measured the sizes of both cerebellar and neocortical organoids in brightfield images at D10, D20, D30, D50, D70, and D90. Interestingly, for both brain region-specific organoid differentiations, we found significant differences in size between PCH2a and control organoids (Figure 3A-C, Supplementary Figure 2A,B,C). Cerebellar organoids demonstrated reduced size compared to controls starting from D10 of differentiation (Figure 3B), while neocortical organoids showed differences from D30 onwards (Figure 3C). At D50, the ratio between the mean sizes of control / PCH2a cerebellar organoids was 1.85, increasing to 3.12 at D90 (Figure 3D). In neocortical organoids, the ratio between the mean sizes of control and PCH2a organoids was 1.13 at D50 and 1.74 at D90 of differentiation (Figure 3D). The brain region-specific organoid growth curves resemble brain morphometry in affected individuals with PCH2a with early detection of cerebellar hypoplasia in the first months of life (Sanchez-Albisua et al., 2014) and the later progressive microcephaly (Ekert et al., 2016).

PCH2a-derived iPSCs differentiate towards cerebellar and neocortical fate

To start assessing the cellular underpinnings of the brain region-specific growth deficits (Figure 3), we analyzed the presence of different progenitor and neuronal cell types in cerebellar and neocortical organoids at different time points. We found robust neural differentiation in PCH2a and control cerebellar organoids based on immunohistochemical analysis for the markers SOX2 (neural progenitor cells) and Tuj1 (immature neurons) at D30. Moreover, organoids acquired a cerebellar fate based on the expression of the glutamatergic cerebellar precursor marker BAHRL1 (Figure 4A,B) and the GABAergic cerebellar precursor marker KIRREL2 in immunohistochemistry at D30 (Figure 4C,D). At later stages of differentiation (D90), we found Calbindin and MAP2-positive cells, indicating the presence of Purkinje cells in cerebellar organoids (Figure 4E,F). Similarly, in neocortical organoids, immunohistochemical analysis for CTIP2, SATB2, SOX2, and Tuj1 revealed neuronal differentiation (Figure 5A-D). We found expression of the neural progenitor marker SOX2 in rosettes surrounded by CTIP2-positive deep layer neurons at D50 in control (Figure 5A) and PCH2a (Figure 5B) neocortical organoids. In addition, expression of the upper layer neuronal marker SATB2 was found at D70 (Figure 5C,D). Taken together, the acquisition of brain region-specific fate and neuronal maturation was evident in both cerebellar and neocortical control and PCH2a organoids, suggesting they can be used to analyze molecular and cellular changes induced by the disease-causing mutation.

Expression of apoptotic marker cleaved Caspase-3 is not altered in PCH2a cerebellar and neocortical organoids

Previous studies on human samples and animal models indicated that hypoplasia results from degeneration and cell death, respectively (Barth et al., 2007; Kasher et al., 2011; Schmidt et al., 2022). We therefore investigated whether elevated levels of apoptosis could explain the reduced size of PCH2a cerebellar and neocortical organoids. However, immunohistochemistry for the apoptotic marker cleaved caspase-3 (cCas3) did not reveal differences between control (Figure 6A,C,E,G) and PCH2a (Figure 6B,D,F,H) organoids at D30 and D50 in both brain-region specific organoid differentiations. Furthermore, quantitative analysis of the cCas3-positive area over the DAPI signal of individual regions of interest (Sox2-rich structures) did not show a significant difference between PCH2a and control organoids at any time point in both cerebellar and neocortical organoids (Figure 6I,J). Taken together, we observe a significant size difference in PCH2a organoids (Figure 3B-D) in the absence of obvious changes in apoptosis at D30 and D50 of differentiation in cerebellar and neocortical organoids (Figure 6).

Discussion

Elucidation of the cellular and molecular mechanisms underlying PCH has been hampered to date by the lack of a model recapitulating specific neuroanatomical hallmarks of the disorder. Here, we have generated human organoid models of PCH2a that recapitulate the brain region-specific pathology observed in affected individuals.

Organoid models used to study neurogenetic disorders

Human brain organoid models have been used extensively to study neurogenetic disorders in a human cellular context (Khakipoor et al., 2020; Velasco et al., 2020). In most cases, organoid models of the neocortex have been employed, even when the cerebellum was primarily affected by the disorder (Bras et al., 2022) since cerebellar differentiation protocols have been developed only recently (Hua et al., 2022; Muguruma et al., 2015; Nayler et al., 2021; Silva et al., 2020). Therefore, to date, the use of cerebellar

organoids in disease modeling has not been demonstrated. In this study, we show the importance of using brain region-specific organoids to model the brain region-specific neuropathology of PCH2a, a severe neurological disorder that primarily affects the cerebellum and pons and, to a lesser extent, the neocortex. PCH2a iPSCs robustly differentiated into both forebrain and hindbrain fate (Figures 4, 5) in line with the observation in *tsen54* loss of function zebrafish experiments, where no defect in specification of different brain regions was found (Kasher et al., 2011). Our results indicate that using organoid protocols of brain regions not primarily affected to study neuropathology may reveal some insights into disease mechanisms. However, the full potential of organoid technology may only be realized by combining different brain region-specific organoids.

Brain region-specific pathology recapitulated in organoids

We find that cerebellar PCH2a organoids are severely reduced in size from early stages on, while neocortical PCH2a organoids start displaying differences in growth at later stages of development (Figure 3). Additionally, differences in cerebellar organoid size between PCH2a and controls at later stages are larger compared to neocortical PCH2a and control organoids (Figure 3). Analogously, in affected individuals, reduced cerebellum size is already present at birth, while a progressive reduction of cerebral volumes may be detected with time, suggesting an ongoing atrophic process of neurodegeneration (Ekert et al., 2016). The atrophy of supratentorial structures in humans could be either caused by a primary effect of the disease-causing variant or as a consequence of the lack of inputs from the cerebellum, as has been discussed in very preterm infants with cerebellar lesions (Limperopoulos et al., 2014). Our data indicate that the disease-causing *TSEN54* variant directly affects neocortical development. Together, primary and secondary effects of the variant on cerebellar and neocortical development may contribute to the diverse symptoms in PCH2a patients. Notably, just 20% of the human cerebellum is involved in motor function (Haldipur et al., 2022; Marek et al., 2018), and cerebellar hypoplasia disrupting cerebellar-cerebral projections may, thus, also contribute directly to the pathological hallmarks of PCH2 not related to motor function, such as neurodevelopmental delay and lack of language development.

Novel insights into the disease mechanism of PCH2a using the organoid models

Our model provides the foundation for studying cellular and molecular disease mechanisms underlying PCH2a as we can generate biomaterial with brain region-specific fate for subsequent analysis of the biochemical and cellular differences. Elucidating disease mechanisms of PCH2a has implications for several rare neurological disorders caused by defects in tRNA processing that lead to neurodegeneration. Mutations in *TSEN54* lead to aberrant tRNA pools in human fibroblasts (Sekulovski et al., 2021). Assuming aberrant tRNA pools are also present in the cerebellar and neocortical PCH2a organoids generated in this study, it remains elusive how altered tRNA pools translate to the reduced size in PCH2a organoids resembling the clinical phenotype of affected individuals. Interestingly, in different systems, tRNAs can directly regulate apoptosis (Avcilar-Kucukgoze and Kashina, 2020; Mei et al., 2010). Neurodegeneration and apoptosis have been suggested to occur in the cerebellum of affected individuals with PCH based on neuropathological observations (Barth et al., 2007) and in animal models of PCH (Ishimura et al., 2014; Kasher et al., 2011; Schmidt et al., 2022), respectively. However, our analysis of cCas3-positive cells did not reveal any differences in apoptosis between PCH2a and control cerebellar and neocortical organoids at D30 and D50. It is possible that at later stages of organoid differentiation apoptosis would be observed in line with the degeneration reported in affected individuals (Barth et al., 2007). Alternatively, we suggest

that the small size of the cerebellar, and to some extent, neocortical organoids, may be caused by deficits in the proliferation of progenitor cells. Supporting the hypothesis that impaired proliferation and differentiation in the cerebellum leads to hypoplasia, bi-allelic variants in *PRDM13* (OMIM *6167441) cause cerebellar hypoplasia in humans (OMIM #619909) and loss of function of *prdm13* disrupts Purkinje cell differentiation in zebrafish (Coolen et al., 2022). Moreover, altered development in several brain structures has been reported in human brain samples of a subtype of PCH (Patel et al., 2006). Mechanistically, specific tRNAs can change cell state and regulate proliferation and differentiation in concert with mRNAs (Gingold et al., 2014). Interestingly, in cancer, specific tRNAs can even promote metastatic progression (Goodarzi et al., 2016). However, how would such changes in tRNA processing lead to brain region-specific pathology? In yeast, deficits in tRNAs are not problematic under normal conditions, however, when challenged additional phenotypes were observed (Bloom-Ackermann et al., 2014). We, therefore, propose that the developing cerebellum and, to a lesser extent, the developing neocortex have specific requirements for appropriate tRNA pools, originating perhaps from the increased neuronal output (Haldipur et al., 2022; Miller et al., 2019). It has been suggested that TSEN is required for processing cerebellum-specific pre-tRNAs (Sekulovski et al., 2021). Indeed, tRNA isodecoders display tissue-specific expression (Ishimura et al., 2014; Pinkard et al., 2020) and tRNA modifications change as oligodendrocyte precursor cells differentiate into oligodendrocytes (Martin et al., 2022), indicating that tRNA pools may be important regulators of neural lineage progression.

Future directions

The homozygous founder variant c.919G>T in the *TSEN54* gene results in the hypomorphic phenotype referred to as PCH2a. Sekulovski and colleagues corroborated this finding showing that the genotype underlying PCH2a does not cause the loss of catalytic activity of TSEN54 but instead causes thermal destabilization (Sekulovski et al., 2021). Truncating variants in a compound heterozygous state with the hypomorphic founder variant or other rare missense variants in *TSEN54* lead to an aggravated phenotype defined as PCH4 and PCH5 (Budde et al., 2008; Namavar et al., 2011b). Taken together, we suggest that TSEN54 malfunction in humans has a graded effect. Animal loss of function models show a loss of neural tissue together with lethality early in development (Ermakova et al., 2018; Kasher et al., 2011; Schmidt et al., 2022), perhaps similar to the phenotype of PCH4 and PCH5 (Budde et al., 2008; Namavar et al., 2011b). However, early death and extensive apoptosis in these models preclude the detailed analysis of disease mechanisms underlying PCH2a, the most common form of PCH, as no material is available for biochemical assays. Especially when modeling neurological disorders, it is essential to consider evolutionary changes between model organisms and our species. The human brain has changed drastically in evolution (Herculano-Houzel, 2012). The neocortex is significantly expanded in size due to changes in the proliferation of neural progenitor cells during prenatal brain development (Geschwind and Rakic, 2013; Miller et al., 2019). Evolutionary changes in the development of cerebellum have been less investigated to date, but profound differences also exist here (Haldipur et al., 2022). We expect that further analysis of disease mechanisms in our human brain region-specific organoid models will elucidate the cellular and molecular underpinnings of the human phenotype and reveal how progenitor proliferation and the differentiation into diverse lineages are affected in the neocortex and cerebellum in PCH2a. Moreover, our study indicates that generating cerebellar organoids as disease models will likely contribute to our understanding of other neurological disorders that differentially affect the cerebellum.

Acknowledgements

We thank the affected individuals and their families for donating samples. We would like to thank PCH-Familie e.V. for their support, especially Julia Matilainen and Axel Lankenau, for the fruitful discussions. We thank Clemens Lumper, Elisabeth Gustafsson, Lea Fischer, Jasmin Treu, Maximilian Feige, Christina Kulka, Ezgi Atay, Felix Hildebrand, Melanie Kraft, and Yvonne Schelling for technical support. RNA of the hESC line I3 and H9 was kindly provided by the Institute of Reconstructive Neurobiology, Bonn, Germany. We thank Javier Martinez, Stefan Weitzer, and Hansjürgen Volkmer for critical feedback on the manuscript.

Funding

We are grateful for financial support from PCH-Familie e.V., the Hertie Foundation, the Baden-Württemberg state postgraduate fellowship (to KS and TK), the Heidelberger Akademie der Wissenschaften (WIN Kolleg), and the Daimler and Benz Foundation (32-06/20, to SM). LS, SG and IK-M are members of the European Reference Network for Rare Neurological Diseases (ERN-RND) – Project ID No 739510.

Conflict of Interest

The authors declare that they have no conflict of interest.

Contributions

TK designed the study, performed experiments, data analysis, and statistical analysis, and prepared the manuscript; SH generated iPSC lines, KS, ZY and KB performed experiments; LL, SG, WJ, and IKM provided clinical expertise and data, LS supervised the generation of iPSC lines, all authors revised the manuscript, SM conceived and designed the study, supervised the work, and prepared the manuscript.

Methods

Recruitment of affected individuals

Affected individuals were recruited within our PCH2 natural history study, collecting clinical and diagnostic data, including diagnostic MR images. Written informed consent was obtained from guardians and archived. All procedures were performed in accordance with the Helsinki Declaration. Individual-level data were de-identified. The study was approved by the ethics committee of the medical faculty by the local Institutional Review Boards of the Medical Faculty of the University of Tübingen, Germany (961/2020BO2 and 598/2011BO1) and Freiburg, Germany (20-1040).

Diagnostic confirmation by genetic sequencing

Next-generation sequencing and/or Sanger sequencing was performed after obtaining written informed consent for either clinical sequencing and/or center-specific institutional review board-approved research sequencing. All affected individuals harbored the hypomorphic founder variant c.919G>T in *TSEN54* in the homozygous state. The bi-allelic localization was confirmed by carrier testing.

Skin biopsies

Skin biopsies were acquired at different ages (9 months to 15 years) according to local standards of routine diagnostic procedures.

Culturing and reprogramming fibroblasts

Human dermal fibroblasts were obtained from skin biopsies and cultivated in Dulbecco's modified eagle medium (DMEM) (Thermo Fisher Scientific) supplemented with 10% fetal bovine serum (FBS) (Thermo Fisher Scientific) (fibroblast medium).

iPSC generation from fibroblasts was performed according to a published protocol with minor modifications (Okita et al., 2013)**.** Briefly, reprogramming was initiated by nucleofection of $1x10^5$ fibroblast with 1 µg of each episomal plasmid (pCXLE-hUL, pCXLE-hSK and pCXLE-hOCT4) using the Nucleofector 2b (Lonza). Initially, fibroblasts were cultivated in fibroblast medium supplemented with 2 ng/ml FGF2 (Peprotech, Cat. no. 100-18B). On D3, the medium was changed to Essential 8 (E8) medium containing 100 µM sodium butyrate (NaB, Sigma-Aldrich, Cat. no. B5887). After 3 – 4 weeks, with media changes every other day, iPSC colonies were manually picked and further expanded in E8 medium performing media changes daily. After ≥5 passages, they were genomically and functionally characterized and frozen in E8 medium containing 40% KO-SR (Thermo Fisher Scientific, Cat. no. 10828-028), 10% DMSO (Sigma-Aldrich, Cat. no. D4540) and 1 µM Y-27632 (Selleck Chemicals, Cat. no. S1049). All iPSC lines used in this study (3 control lines, 3 PCH2a lines) were characterized according to the scientific guidelines for Lab Resources (Stem Cell Research).

Genomic integrity analysis

To verify genomic integrity, DNA of iPSCs and fibroblasts was isolated with DNeasy Blood & Tissue Kit (Qiagen) according to the manufacturer's guidelines. Whole-genome SNP genotyping (SNP array) was conducted using Infinium OmniExpressExome-8-BeadChip (Illumina) and GenomeStudio V2.0.3 (Illumina) for evaluation. Copy number analysis was performed using CNVPartition plugin (Illumina). Early mosaicism states were evaluated by manual review of B allele frequency plots on a chromosomal level.

Pluripotency assessment

To assess the alkaline phosphatase (ALP) expression or for immunocytochemical analysis, iPSCs were fixed with 4% paraformaldehyde (PFA) and either assessed for ALP expression or permeabilized with 0.1% Triton X-100, blocked with 5% FBS and stained overnight at 4°C with primary antibodies for immunocytochemical analysis (rabbit anti-OCT4, 1:100, Proteintech, Cat. no. 11263-1-AP / mouse anti-TRA-1-81, 1:500, Millipore, Cat. no. MAB4381). Samples were visualized after staining with Alexa Fluor 488-conjugated secondary antibodies (Thermo Fisher Scientific) for 1h at room temperature. Nuclei were counterstained with Hoechst 33342 (1:10.000, Invitrogen). Samples were embedded in ProLong Gold Antifade Reagent (Thermo Fisher Scientific, Cat. No. P36930) and imaged with AxioImager Z1 (Zeiss).

On RNA level, qRT-PCR with primers specific for pluripotency genes (*OCT3/4, SOX2, KLF4, cMYC, NANOG, DNMT3B*) was performed: RNA of iPSCs was isolated with RNeasy Mini Kit (Qiagen) according to manufacturer's guidelines and reverse-transcribed to cDNA, using RevertAid First Strand cDNA Synthesis Kit (Thermo Fisher Scientific). Quantitative real-time PCR was performed in triplicate per sample and primer by adding 3 µL cDNA (1.25 ng/µL) to 2 µL primer pairs (2 µM) and 5 µL SYBR Green Select Master Mix (Applied Biosystems) using the ViiA 7 Real-Time PCR System (Applied Biosystems). *GAPDH* and *TBP* were used as housekeeping genes, and relative quantification (RQ) values (RQ_{min}/RQ_{max}) were determined

by comparing the expression levels to hESCs (I3, H9) and fibroblasts. The following primers were used (forward / reverse):

Gene	Direction	Sequence
OCT3/4	f	GGAAGGTATTCAGCCAAACG
	r	CTCCAGGTTGCCTCTCACTC
c-MYC	f	ATTCTCTGCTCTCCTCGACG
	r	CTGTGAGGAGGTTTGCTGTG
KLF4	f	CCATCTTTCTCCACGTTCGC
	r	CGTTGAACTCCTCGGTCTCT
SOX2	f	TGATGGAGACGGAGCTGAAG
	r	GCTTGCTGATCTCCGAGTTG
NANOG	f	CAAAGGCAAACAACCCACTT
	r	TGCGTCACACCATTGCTATT
DNMT3B	f	ACGACACAGAGGACACACAT
	r	AAGCCCTTGATCTTTCCCCA
GAPDH	f	AGGTCGGAGTCAACGGATTT
	r	ATCTCGCTCCTGGAAGATGG

The differentiation capacity of iPSCs into cells of all three germ layers was determined by an embryonic body (EB)-based protocol. $1.2x10^6$ iPSCs were seeded in AggreWell800 plates (Stem cell technologies) in EB medium consisting of DMEM/F-12 supplemented with 20% Knockout Serum Replacement, 1% MEM Non-essential-amino-acid solution, 1% Pen/Strep, 1% GlutaMAX and 50µM β-Mercaptoethanol. On D4, EBs were plated onto coverslips for further differentiation. Specific marker expression (TUJ (mouse anti-TUJ, 1:1,000, Sigma Aldrich, Cat. no. T8660), SMA (mouse anti-SMA, 1:100, Dako, Cat. no. M0851) was assessed after 10 days as described above. For endodermal induction of iPSCs, $2x10^5$ cells were seeded onto coverslips and cultivated in endoderm induction medium consisting of RPMI1640 advanced supplemented with 1xB27, 1% Pen/Strep, 0.2% FCS, 2µM CHIR-99021 and 50ng/ml Activin A. At D4 of differentiation, cells were stained for FOXA2 (rabbit anti-FOXA2, 1:300, Millipore, Cat. no. 07-633), following the fixation and immunocytochemistry protocol mentioned above.

iPSC culture

iPSC lines derived from affected individuals and control lines were generated following the same protocol and cultured under standard conditions (37°C, 5% CO2, and 100% humidity) in E8 Flex medium (Gibco, Cat. no. A2858501) on hESC-qualified growth factor-reduced Matrigel-coated (Corning, Cat. no. 354277) cell culture dishes (Greiner, Cat. no. 657160). Passaging was performed in colonies using Gentle Dissociation Reagent (STEMCELL Technologies, Cat. no. 07174) once the culture reached 80%-90% confluency. The culture medium was supplemented with Thiazovivin (Sigma-Aldrich, Cat. no. 420220) until the following day. All cell lines were tested for mycoplasma contamination regularly with PCR Mycoplasma Detection Set (TaKaRa, Cat. no. 6601) and maintained under passage 30. The pluripotency for each cell line was confirmed with antibodies against OCT4 (rabbit, 1:500, Abcam, Cat. no. ab19857) before each differentiation.

Generation of cerebellar organoids

Cerebellar organoids were generated as previously described (Silva et al., 2020) with some alterations: 80-90% confluent iPSCs were dissociated into single cells using Accutase (Merck, Cat. no. A6964), and 4,500 cells were seeded per well of 96 well V-bottom low adhesion plates (S-bio, Cat. no. MS-9096VZ) in E8 Flex medium (Gibco, Cat. no. A2858501), supplemented with 10 µM Y-27632 (Cayman Chemical, Cat. no. 10005583). Once the aggregates reached a diameter of 250 µm, the medium was changed to growth factor-free chemically defined medium (gfCDM), supplemented with 50 ng/ml FGF2 (PeproTech, Cat. no. 100-18B) and 10 µM SB-431542 (Tocris, Cat. No. 1614). At D7 of differentiation, FGF2 and SB-431542 were reduced to 33.3 ng/ml and 6.67 µM, respectively. At D14, media was supplemented with 100 ng/ml FGF19 (PeproTech, Cat. No. 100-32). The medium was changed to Neurobasal Medium at D21, supplemented with 300 ng/ml SDF-1 from D28 to D34. From D35 onwards, media was changed to complete BrainPhys (StemCell Technologies, Cat. No. 5793), supplemented with 10 µg/ml BDNF (PeproTech, Cat.No. 450-02), 100 µg/ml GDNF (PeproTech, Cat.No. 450-10), 100 mg/ml dbcAMP (PeproTech, Cat.No. 1698950) and 250 mM ascorbic acid (Tocris, Cat. No. 4055).

Generation of cortical spheroids

Cortical spheroids were generated as previously described (Pasca et al., 2015) with only minor alterations. In brief, 80-90% confluent iPSCs were dissociated into single cells using Accutase (Merck, Cat. no A6964) and 9000 cells were seeded per well of 96 well V-bottom low adhesion plates (S-bio, Cat. no. MS-9096VZ) in E8 Flex medium (Gibco, Cat. no. A2858501) supplemented with 10 µM Y-27632 (Cayman Chemical, Cat. no. 10005583). The medium was changed to neural induction medium (NI) (Essential 6 Thermo Fisher Cat. No. A151640), supplemented with 2.5 µM Dorsomorphin (Tocris, Cat. No. 3093), 10 µM SB-431542 (Tocris, Cat. No. 1614) and 2.5 µM XAV-939 (Tocris, Cat. No. 3748) the next day. NI medium was changed every other day and replaced with neural maintenance medium (NM) (Neurobasal-A (Gibco, Cat. no.10888-022), B27-VitA (Thermo Fisher, Cat. no. 12587010), GlutaMAX (Thermo Fisher, Cat. no. 35050038), Pen/Strep (Sigma, Cat. no. P0781) at D6. NM was supplemented with 20 ng/ml EGF (Merck, Cat. No GF144) and FGF2 (PeproTech, Cat. No. 100-18B) from D6 to D24 and with 20 ng/ml BDNF (PeproTech, Cat. No. 450-02) and NT-3 (PeproTech, Cat. No. 450-03) from D25 to D43. NM was changed every other day and not supplemented after D43.

Size measurements

To investigate the size of organoids, brightfield images of the organoids were taken at D0, D10, D20, D30, D50, D70 and D90 of differentiation with an EVOS cell imaging system (Thermo Fisher). These images were analyzed using a published macro (Ivanov et al., 2014) for FIJI (Schindelin et al., 2012). The data were further analyzed with Excel, and Graph Pad Prism was used to plot data.

Fixation, cryosections and immunohistochemistry

Organoids were fixed at respective time points in 4% paraformaldehyde (PFA, Morphisto, Cat. no. 11762) in PBS for 45–60 min at room temperature (Lancaster and Knoblich, 2014). The organoids were washed three times for 15 minutes with 1x PBS (Roth, Cat. no. 1105.1) and then incubated in 30% sucrose (Sigma Aldrich, Cat. no. S7903) in PBS solution at 4°C until they sunk to the bottom of the dish. The organoids were embedded in a 1:1 v/v mixture of 30% sucrose in PBS and optimal cutting temperature (OCT)

compound (Sakura, Cat. no. 4583) and sectioned on Superfrost Plus slides (R. Langenbrinck GmbH, Cat. no 03-0060) with a cryostat at 20 µm (Leica). The slides were stored at -80°C.

For immunohistochemistry, slides were thawed for 15 minutes at room temperature and the embedding solution was rinsed off with PBS. Antigen retrieval was achieved by immersing the slides in 10 mM citric acid buffer (pH 6.0) and boiling for 20 minutes in a microwave. A hydrophobic pen (PAP pen, Abcam, Cat. no. ab2601) was used to circle the sections to prevent the blocking solution from spilling during incubation. Permeabilization and blocking were performed with 1% Triton-X100 (Sigma, Cat. No. T8787), 0.2% gelatin (Sigma, Cat. no. G1890), and 10% normal donkey serum (Abcam, Cat. no. ab7475) in PBS for 1 hour at room temperature. Primary antibodies were diluted in permeabilization and blocking solution and applied to the sections overnight at 4°C. Subsequently, the slides were rinsed with PBS three times for 15 minutes, then secondary antibodies were diluted in permeabilization and blocking solution and applied for three hours at room temperature. The sections were rinsed in PBS three times for 15 minutes, and nuclei were stained with DAPI (1:5000) (Thermofisher Scientific, Cat. no. D1306) diluted in PBS for 4 minutes, rinsed in PBS and mounted using ProLong Gold (Thermofisher Scientific, Cat. no. P36930).

Whole-mount immunohistochemistry and clearing of organoids

To stain whole organoids, we used an established whole mount staining protocol (Lee et al., 2016a). Primary antibodies were diluted in 3D blocking solution consisting of PBS with 6% (v/v) BSA (Gibco, Cat. no. 11500496), 0.5% (v/v) Triton X-100, 0.1% (w/v) Sodium azide (Sigma-Aldrich, Cat. no. S2002) and 1% (v/v) Pen/Strep (Merck, Cat. no. P0781). The samples were incubated with the primary antibodies for 6 days at 37°C, changing the antibody solution once in between. Organoids were washed 5 times with 0.1% Triton X-100 in PBS at 1 hour intervals. Subsequently, secondary antibodies and DAPI (1:5000) diluted in 3D blocking solution were added and organoids were incubated for 6 days, changing the solution once. Lastly, the samples were washed 5 times with 0.1% Triton X-100 in PBS at 1h intervals.

After the staining procedure, optical clearing of the tissue with the Benzylalcohol/Benzylbenzoat (BABB, Sigma-Aldrich, Cat. no. 305187; Thermo Fisher, Cat. no. 105862500) was performed (Dent et al., 1989). First, the samples were dehydrated in an ascending methanol row of 25%, 50%, 75% and 100% (v/v) methanol (Honeywell, Cat. no. 32213) in PBS. Subsequently, the organoids were transferred to Screenstar COC flat bottom plates (Greiner, Cat. no. 655866) and incubated in BABB/methanol solution (25% BA, 25% BB, 50% methanol) for 30 minutes. Lastly, the solution was changed to 100% BABB and the organoids were kept in this solution for subsequent imaging.

Primary Antibodies

Antibody	**species**	**vendor**	**cat number**	**dilution**
BAHRL1	rabbit	HPA	HPA004809	1:500
Calbindin	mouse	Merck	C9848	1:500
cCas3	rabbit	CST	9661S	1:400
CTIP2	rat	Abcam	ab18465	1:500
Ki67	rabbit	Merck	AB9260	1:600
KIRREL2	rabbit	HPA	HPA071587	1:500
Map2	rabbit	Abcam	ab32454	1:500

Oct4	rabbit	Abcam	ab19857	1:500
Satb2	rabbit	Abcam	ab34735	1:500
Sox2	goat	R&D Systems	AF2018	1:500
TSEN54	rabbit	Invitrogen	PA5-101939	1:500
Tuj1	mouse	HPA	AMAb91394	1:500

Secondary antibodies

Host species	Target species	Em wavelength	Provider	Cat.no
donkey	goat	AF555	Abcam	ab150130
donkey	goat	AF647	Abcam	A21447
donkey	mouse	AF568	Abcam	ab175472
donkey	mouse	AF647	Abcam	A31571
donkey	rabbit	AF488	Abcam	A21206
donkey	rabbit	AF546	Abcam	A10040
donkey	rabbit	AF647	Abcam	A31573
donkey	sheep	AF488	Abcam	A11015
donkey	sheep	AF647	Abcam	A21448

Sanger sequencing

To ensure the correct genetic background of all iPSC lines and control, Sanger sequencing was performed. Genomic DNA was extracted using DNA isolate kit (BioCat, Cat. No. BIO-52066-BL). The region of interest was amplified using Phusion® High-Fidelity PCR Kit (New England Biolabs, Cat. No. E0553S). The PCR product was purified with QIAquick PCR Purification Kit (Qiagen, Cat. No. 28104), and samples were sent to Eurofins for sequencing. The following primers were used: Forward (AGAAACCCCAGGAGT), reverse (CTCAATCCATCCGAG).

RNA isolation, cDNA synthesis and qPCR

To Isolate RNA of iPSCs and Organoids, RNeasy Mini Kit (Qiagen, Cat.No. 74106) was used according to manufacturers' advice. Organoid samples were pooled (n=20) to ensure sufficient yield. Synthesis of cDNA was performed with EvoScript Universal cDNA Master (Roche, Cat. No. 7912455001). For qPCR, the LightCycler® 480 SYBR Green I Master Kit (Roche Cat. No. 4887352001) and the LightCycler 96 (Roche) were used. Samples were processed in triplicates. The qPCR data were analysed with the respective program (LicghtCycler 96, Roche). *GAPDH* was used as a housekeeping gene, and the data was analyzed following ΔΔCt method using D0 for each line as a normalization control. qPCR Primers for *TSEN54* were generated with the primer-BLAST tool, with WT TSEN54 being the gene of interest (https://www.ncbi.nlm.nih.gov/tools/primer-blast/). Additionally, published primers were used (see below).

qRT-PCR primers

Gene	Direction	Sequence	Reference
TSEN54	f	GAAGTCTGGGGCTTGGAAA	
	r	CACATCCGGGCATAGGTT	
GAPDH	f	GAACGGGAAGCTTGTCATCAA	(Pasca et al., 2015)
	r	ATCGCCCCACTTGATTTTGG	

Quantification of cCas3 staining

To quantify the cCas3 positive area of regions of interest within individual organoids, we stained and imaged respective samples in one experiment. The laser intensity of the confocal microscope was adjusted according to the negative staining control. All samples were imaged with the same laser intensity settings. Raw image files were further processed in FIJI (Schindelin et al., 2012). To analyze the area of stained cells, thresholding for DAPI and cCas3 channels was performed with identical parameters for each channel and all samples. First, the area of positively stained regions was quantified using the "measure" tool in FIJI. Then the cCas3 area was normalized to the DAPI-positive area of the respective image. Finally, statistical analysis and plotting were performed in GraphPad Prism.

References

Aldinger, K.A., Thomson, Z., Phelps, I.G., Haldipur, P., Deng, M., Timms, A.E., Hirano, M., Santpere, G., Roco, C., Rosenberg, A.B.*, et al.* (2021). Spatial and cell type transcriptional landscape of human cerebellar development. Nat Neurosci *24*, 1163-1175.

Ammann-Schnell, L., Groeschel, S., Kehrer, C., Frolich, S., and Krageloh-Mann, I. (2021). The impact of severe rare chronic neurological disease in childhood on the quality of life of families-a study on MLD and PCH2. Orphanet J Rare Dis *16*, 211.

Avcilar-Kucukgoze, I., and Kashina, A. (2020). Hijacking tRNAs From Translation: Regulatory Functions of tRNAs in Mammalian Cell Physiology. Front Mol Biosci *7*, 610617.

Barth, P.G., Aronica, E., de Vries, L., Nikkels, P.G., Scheper, W., Hoozemans, J.J., Poll-The, B.T., and Troost, D. (2007). Pontocerebellar hypoplasia type 2: a neuropathological update. Acta Neuropathol *114*, 373-386.

Bloom-Ackermann, Z., Navon, S., Gingold, H., Towers, R., Pilpel, Y., and Dahan, O. (2014). A comprehensive tRNA deletion library unravels the genetic architecture of the tRNA pool. PLoS Genet *10*, e1004084.

Bras, J., Henriques, D., Moreira, R., Santana, M.M., Silva-Pedrosa, R., Adao, D., Braz, S., Alvaro, A.R., de Almeida, L.P., and Mendonca, L.S. (2022). Establishment and characterization of human pluripotent stem cells-derived brain organoids to model cerebellar diseases. Sci Rep *12*, 12513.

Budde, B.S., Namavar, Y., Barth, P.G., Poll-The, B.T., Nurnberg, G., Becker, C., van Ruissen, F., Weterman, M.A., Fluiter, K., te Beek, E.T.*, et al.* (2008). tRNA splicing endonuclease mutations cause pontocerebellar hypoplasia. Nat Genet *40*, 1113-1118.

Chan, P.P., and Lowe, T.M. (2009). GtRNAdb: a database of transfer RNA genes detected in genomic sequence. Nucleic Acids Res *37*, D93-97.

Coolen, M., Altin, N., Rajamani, K., Pereira, E., Siquier-Pernet, K., Puig Lombardi, E., Moreno, N., Barcia, G., Yvert, M., Laquerriere, A.*, et al.* (2022). Recessive PRDM13 mutations cause fatal perinatal brainstem

dysfunction with cerebellar hypoplasia and disrupt Purkinje cell differentiation. Am J Hum Genet *109*, 909-927.
Dent, J.A., Polson, A.G., and Klymkowsky, M.W. (1989). A whole-mount immunocytochemical analysis of the expression of the intermediate filament protein vimentin in Xenopus. Development *105*, 61-74.
Ekert, K., Groeschel, S., Sanchez-Albisua, I., Frolich, S., Dieckmann, A., Engel, C., and Krageloh-Mann, I. (2016). Brain morphometry in Pontocerebellar Hypoplasia type 2. Orphanet J Rare Dis *11*, 100.
Ermakova, O., Orsini, T., Gambadoro, A., Chiani, F., and Tocchini-Valentini, G.P. (2018). Three-dimensional microCT imaging of murine embryonic development from immediate post-implantation to organogenesis: application for phenotyping analysis of early embryonic lethality in mutant animals. Mamm Genome *29*, 245-259.
Geschwind, D.H., and Rakic, P. (2013). Cortical evolution: judge the brain by its cover. Neuron *80*, 633-647.
Gingold, H., Tehler, D., Christoffersen, N.R., Nielsen, M.M., Asmar, F., Kooistra, S.M., Christophersen, N.S., Christensen, L.L., Borre, M., Sorensen, K.D*., et al.* (2014). A dual program for translation regulation in cellular proliferation and differentiation. Cell *158*, 1281-1292.
Goodarzi, H., Nguyen, H.C.B., Zhang, S., Dill, B.D., Molina, H., and Tavazoie, S.F. (2016). Modulated Expression of Specific tRNAs Drives Gene Expression and Cancer Progression. Cell *165*, 1416-1427.
Haldipur, P., Millen, K.J., and Aldinger, K.A. (2022). Human Cerebellar Development and Transcriptomics: Implications for Neurodevelopmental Disorders. Annu Rev Neurosci *45*, 515-531.
Hayne, C.K., Lewis, T.A., and Stanley, R.E. (2022). Recent insights into the structure, function, and regulation of the eukaryotic transfer RNA splicing endonuclease complex. Wiley Interdiscip Rev RNA *13*, e1717.
Herculano-Houzel, S. (2012). Neuronal scaling rules for primate brains: the primate advantage. Prog Brain Res *195*, 325-340.
Hua, T., Liu, C., Kiran, S., Gray, K., Jung, S., Meckes, D.G., Jr., Li, Y., and Sang, Q.A. (2022). Phenotypic, metabolic, and biogenesis properties of human stem cell-derived cerebellar spheroids. Sci Rep *12*, 12880.
Ishimura, R., Nagy, G., Dotu, I., Zhou, H., Yang, X.L., Schimmel, P., Senju, S., Nishimura, Y., Chuang, J.H., and Ackerman, S.L. (2014). RNA function. Ribosome stalling induced by mutation of a CNS-specific tRNA causes neurodegeneration. Science *345*, 455-459.
Ivanov, D.P., Parker, T.L., Walker, D.A., Alexander, C., Ashford, M.B., Gellert, P.R., and Garnett, M.C. (2014). Multiplexing spheroid volume, resazurin and acid phosphatase viability assays for high-throughput screening of tumour spheroids and stem cell neurospheres. PLoS One *9*, e103817.
Kang, H.J., Kawasawa, Y.I., Cheng, F., Zhu, Y., Xu, X., Li, M., Sousa, A.M., Pletikos, M., Meyer, K.A., Sedmak, G*., et al.* (2011). Spatio-temporal transcriptome of the human brain. Nature *478*, 483-489.
Kasher, P.R., Namavar, Y., van Tijn, P., Fluiter, K., Sizarov, A., Kamermans, M., Grierson, A.J., Zivkovic, D., and Baas, F. (2011). Impairment of the tRNA-splicing endonuclease subunit 54 (tsen54) gene causes neurological abnormalities and larval death in zebrafish models of pontocerebellar hypoplasia. Hum Mol Genet *20*, 1574-1584.
Khakipoor, S., Crouch, E.E., and Mayer, S. (2020). Human organoids to model the developing human neocortex in health and disease. Brain Res, 146803.
Korneck, M., Wiora, L., Schols, L., and Hauser, S. (2022). Generation of two SPAST knockout human induced pluripotent stem cell lines to create a model for Hereditary Spastic Paraplegia type 4. Stem Cell Res *60*, 102741.
Lancaster, M.A., and Knoblich, J.A. (2014). Generation of cerebral organoids from human pluripotent stem cells. Nat Protoc *9*, 2329-2340.

Lee, E., Choi, J., Jo, Y., Kim, J.Y., Jang, Y.J., Lee, H.M., Kim, S.Y., Lee, H.J., Cho, K., Jung, N.*, et al.* (2016a). ACT-PRESTO: Rapid and consistent tissue clearing and labeling method for 3-dimensional (3D) imaging. Sci Rep *6*, 18631.

Lee, J.R., Kim, Y.H., Park, S.J., Choe, S.H., Cho, H.M., Lee, S.R., Kim, S.U., Kim, J.S., Sim, B.W., Song, B.S.*, et al.* (2016b). Identification of Alternative Variants and Insertion of the Novel Polymorphic AluYl17 in TSEN54 Gene during Primate Evolution. Int J Genomics *2016*, 1679574.

Limperopoulos, C., Chilingaryan, G., Sullivan, N., Guizard, N., Robertson, R.L., and du Plessis, A.J. (2014). Injury to the premature cerebellum: outcome is related to remote cortical development. Cereb Cortex *24*, 728-736.

Marek, S., Siegel, J.S., Gordon, E.M., Raut, R.V., Gratton, C., Newbold, D.J., Ortega, M., Laumann, T.O., Adeyemo, B., Miller, D.B.*, et al.* (2018). Spatial and Temporal Organization of the Individual Human Cerebellum. Neuron *100*, 977-993 e977.

Martin, S., Allan, K.C., Pinkard, O., Sweet, T., Tesar, P.J., and Coller, J. (2022). Oligodendrocyte differentiation alters tRNA modifications and codon optimality-mediated mRNA decay. Nat Commun *13*, 5003.

Mei, Y., Yong, J., Liu, H., Shi, Y., Meinkoth, J., Dreyfuss, G., and Yang, X. (2010). tRNA binds to cytochrome c and inhibits caspase activation. Mol Cell *37*, 668-678.

Miller, D.J., Bhaduri, A., Sestan, N., and Kriegstein, A. (2019). Shared and derived features of cellular diversity in the human cerebral cortex. Curr Opin Neurobiol *56*, 117-124.

Muguruma, K., Nishiyama, A., Kawakami, H., Hashimoto, K., and Sasai, Y. (2015). Self-organization of polarized cerebellar tissue in 3D culture of human pluripotent stem cells. Cell Rep *10*, 537-550.

Namavar, Y., Barth, P.G., Kasher, P.R., van Ruissen, F., Brockmann, K., Bernert, G., Writzl, K., Ventura, K., Cheng, E.Y., Ferriero, D.M.*, et al.* (2011a). Clinical, neuroradiological and genetic findings in pontocerebellar hypoplasia. Brain *134*, 143-156.

Namavar, Y., Chitayat, D., Barth, P.G., van Ruissen, F., de Wissel, M.B., Poll-The, B.T., Silver, R., and Baas, F. (2011b). TSEN54 mutations cause pontocerebellar hypoplasia type 5. Eur J Hum Genet *19*, 724-726.

Nayler, S., Agarwal, D., Curion, F., Bowden, R., and Becker, E.B.E. (2021). High-resolution transcriptional landscape of xeno-free human induced pluripotent stem cell-derived cerebellar organoids. Sci Rep *11*, 12959.

Nowakowski, T.J., Bhaduri, A., Pollen, A.A., Alvarado, B., Mostajo-Radji, M.A., Di Lullo, E., Haeussler, M., Sandoval-Espinosa, C., Liu, S.J., Velmeshev, D.*, et al.* (2017). Spatiotemporal gene expression trajectories reveal developmental hierarchies of the human cortex. Science *358*, 1318-1323.

Okita, K., Yamakawa, T., Matsumura, Y., Sato, Y., Amano, N., Watanabe, A., Goshima, N., and Yamanaka, S. (2013). An efficient nonviral method to generate integration-free human-induced pluripotent stem cells from cord blood and peripheral blood cells. Stem Cells *31*, 458-466.

Pasca, A.M., Sloan, S.A., Clarke, L.E., Tian, Y., Makinson, C.D., Huber, N., Kim, C.H., Park, J.Y., O'Rourke, N.A., Nguyen, K.D.*, et al.* (2015). Functional cortical neurons and astrocytes from human pluripotent stem cells in 3D culture. Nat Methods *12*, 671-678.

Patel, M.S., Becker, L.E., Toi, A., Armstrong, D.L., and Chitayat, D. (2006). Severe, fetal-onset form of olivopontocerebellar hypoplasia in three sibs: PCH type 5? Am J Med Genet A *140*, 594-603.

Pinkard, O., McFarland, S., Sweet, T., and Coller, J. (2020). Quantitative tRNA-sequencing uncovers metazoan tissue-specific tRNA regulation. Nat Commun *11*, 4104.

Sanchez-Albisua, I., Frolich, S., Barth, P.G., Steinlin, M., and Krageloh-Mann, I. (2014). Natural course of pontocerebellar hypoplasia type 2A. Orphanet J Rare Dis *9*, 70.

Schaffer, A.E., Pinkard, O., and Coller, J.M. (2019). tRNA Metabolism and Neurodevelopmental Disorders. Annu Rev Genomics Hum Genet *20*, 359-387.

Schindelin, J., Arganda-Carreras, I., Frise, E., Kaynig, V., Longair, M., Pietzsch, T., Preibisch, S., Rueden, C., Saalfeld, S., Schmid, B.*, et al.* (2012). Fiji: an open-source platform for biological-image analysis. Nat Methods *9*, 676-682.
Schmidt, C.A., Min, L.Y., McVay, M.H., Giusto, J.D., Brown, J.C., Salzler, H.R., and Matera, A.G. (2022). Mutations in Drosophila tRNA processing factors cause phenotypes similar to Pontocerebellar Hypoplasia. Biol Open *11*.
Sekulovski, S., Devant, P., Panizza, S., Gogakos, T., Pitiriciu, A., Heitmeier, K., Ramsay, E.P., Barth, M., Schmidt, C., Tuschl, T.*, et al.* (2021). Assembly defects of human tRNA splicing endonuclease contribute to impaired pre-tRNA processing in pontocerebellar hypoplasia. Nat Commun *12*, 5610.
Silva, T.P., Fernandes, T.G., Nogueira, D.E.S., Rodrigues, C.A.V., Bekman, E.P., Hashimura, Y., Jung, S., Lee, B., Carmo-Fonseca, M., and Cabral, J.M.S. (2020). Scalable Generation of Mature Cerebellar Organoids from Human Pluripotent Stem Cells and Characterization by Immunostaining. J Vis Exp.
Stork, T., Nessler, J., Anderegg, L., Hunerfauth, E., Schmutz, I., Jagannathan, V., Kyostila, K., Lohi, H., Baumgartner, W., Tipold, A.*, et al.* (2019). TSEN54 missense variant in Standard Schnauzers with leukodystrophy. PLoS Genet *15*, e1008411.
Trotta, C.R., Paushkin, S.V., Patel, M., Li, H., and Peltz, S.W. (2006). Cleavage of pre-tRNAs by the splicing endonuclease requires a composite active site. Nature *441*, 375-377.
Uhlen, M., Fagerberg, L., Hallstrom, B.M., Lindskog, C., Oksvold, P., Mardinoglu, A., Sivertsson, A., Kampf, C., Sjostedt, E., Asplund, A.*, et al.* (2015). Proteomics. Tissue-based map of the human proteome. Science *347*, 1260419.
van Dijk, T., Baas, F., Barth, P.G., and Poll-The, B.T. (2018). What's new in pontocerebellar hypoplasia? An update on genes and subtypes. Orphanet J Rare Dis *13*, 92.
Velasco, S., Paulsen, B., and Arlotta, P. (2020). 3D Brain Organoids: Studying Brain Development and Disease Outside the Embryo. Annu Rev Neurosci *43*, 375-389.
Zhang, Z., O'Laughlin, R., Song, H., and Ming, G.L. (2022). Patterning of brain organoids derived from human pluripotent stem cells. Curr Opin Neurobiol *74*, 102536.

Figure Legends

Figure 1: Generation of PCH2a iPSCs. (A) MRI of the brain of a normally developing infant (6 months old) and (B) an infant with PCH2a (6 months old, donor of iPSC line PCH-2).T2w coronal images (A and B, left) show cerebellar hemispheres severely reduced in size (indicated by arrows) in the PCH2a child compared to the control individual. T1w sagittal images (A and B, right) illustrate the severe pontine and cerebellar hypoplasia in the PCH2a child (indicated by arrows). (C) Experimental scheme of PCH2a iPSC and organoid generation. (D) Alkaline phosphatase (ALP) staining of undifferentiated iPSCs. Immunocytochemical stainings of undifferentiated iPSCs for the pluripotency markers OCT4 (E) and TRA1-81 (F) and DAPI (nuclei) demonstrate the pluripotency of generated cell lines. (G-I) Immunocytochemical staining of spontaneously differentiated iPSCs. Cells were stained for Tuj1 (ß-III-tubulin, ectoderm). (G), SMA (smooth muscle actin, mesoderm) (H), and FOXA2 (Forkhead Box A2, endoderm) (I), as well as DAPI (nuclei), illustrates the differentiation potential of iPSCs. (J) Immunocytochemical staining of PCH2a and control iPSCs for TSEN54 confirms the expression of TSEN54 in all iPSC lines. Th illustration was created with Biorender.

Figure 2: Cerebellar and neocortical organoids express TSEN54. (A) Experimental design of the generation of cerebellar and neocortical organoids. (B) qRT-PCR analysis of RNA expression TSEN54 of iPSCs, neocortical and cerebellar organoids. PCH2a and control organoids do not demonstrate significant differences. Cerebellar and neocortical differentiations do not significantly differ in fold changes from D0 ($p>0.05$ Mann-Whitney test). RNA was isolated from 3 PCH2a and 3 control cell lines, n=20 organoids were pooled for RNA isolation. Data shows technical triplicates per cell line and condition. The bar represents the mean, error bars represent the standard error of the mean (SEM). (C-F) Confocal images of immunohistochemistry against TSEN54 (red) and Tuj1 (green) in cerebellar (C, D) and neocortical (E, F) organoid sections at D50 illustrates the expression of TSEN54 in PCH2a and control organoids throughout the tissue. The illustration was created with Biorender.

Figure 3: **PCH2a organoids are significantly smaller than control organoids.** (A) Representative bright field images of cerebellar and neocortical organoids in culture at D30 and D90 of differentiation illustrate the differences in size. (B, C) Growth curves of PCH2a and control cerebellar (B) and neocortical (C) organoids, differentiated from 3 different cell lines per condition (derived from 3 different individuals), show the area of the organoids in the images pictured in A during the culture period of 90 days. Cerebellar organoids (B) differ significantly in size from D10 of differentiation ($p< 0.05$ unpaired t-test with Welch's correction assuming unequal SDs), with discrepancies increasing over time. Neocortical organoids (C) show significant differences from D30 of differentiation ($p< 0.05$ unpaired t-test with Welch's correction assuming unequal SDs). $n>8$ organoids per cell line, timepoint and differentiation. Points represent the mean, error bars represent SEM. (D) Ratio between mean sizes of control / PCH2a organoids calculated from data presented in (B) and (C). Ratios increase over time and are higher within cerebellar differentiation.

Figure 4: **PCH2a and control cerebellar organoids show differentiation into different neuronal lineages.** (A, B) Single optical slices of confocal images of whole-mount immunohistochemistry on control at D30 (A) and PCH2a D30 (B) cerebellar organoids. Expression of early neuronal marker Tuj1 (green), neural precursor marker SOX2 (red), and glutamatergic precursor marker BAHRL1 (magenta). (C, D) Immunohistochemistry of control (C) and PCH2a (D) cerebellar organoid sections at D30 shows cells positive for the GABA-ergic precursor marker KIRREL2. (E, F) Expression of Calbindin at D90 identifies Purkinje-like cells in control and PCH2a cerebellar organoids.

Figure 5: PCH2a and control neocortical organoids express layer-specific neuronal markers. (A-D) Epifluorescent microscopy images of immunohistochemistry on neocortical organoid sections. Control (A) and PCH2a (B) neocortical organoids express early-born deep-layer neuronal marker CTIP2 at D50 of differentiation. CTIP2-positive cells are organized around SOX2-positive progenitor cells, forming Ventricular zone-like structures. (C, D) Control (C) and PCH2a (D) neocortical organoids show expression of CTIP2 as well upper layer neuronal marker SATB2 at D70 of differentiation.

Figure 6: Apoptotic marker cleaved Caspase 3 (cCas3) is not altered in PCH2a organoids. (A-H): Confocal microscopy images of immunohistochemistry on cerebellar (A-D) and neocortical (E-H) organoid sections at D30 and D50 of differentiation show expression of neural precursor marker SOX2 and apoptotic marker cCas3 in rosette-like structures of organoids. (I, J) Quantification of cCas3 positive area over DAPI signal shows no significant difference in cCas3 expression between PCH2a and control organoids in different brain-region specific organoids and at different time points ($p>0.5$ in Kolmogorov-Smirnov test assuming unequal distribution).

Supplementary Figure 1: Quality control of iPSC generation. (A) qRT-PCR of pluripotency markers of iPSC line PCH-1. GAPDH/TDP were used as housekeeping genes, and relative quantification (RQ) values (RQmin/RQmax) were determined using hESC line H9 as a reference. (B) Sanger sequencing results of previously generated PCH2a and control iPSCs verifies point mutation of PCH2a-derived iPSCs.

Supplementary Figure 2: **Size differences of cerebellar and neocortical organoids at different stages of differentiation.** Cerebellar (A) and neocortical (B) control and PCH2a organoid areas at D30, D50 and D90 of differentiation. Sizes of organoids differ significantly between PCH2a and control organoids. Cerebellar organoids show a higher difference between PCH2a and control than neocortical organoids. ($p < 0.05$ unpaired t-test with Welch's correction assuming unequal SDs). $n > 8$ organoids per cell line, time point and differentiation. (C) The simple linear regression model of cerebellar and neocortical differentiation illustrates the discrepancies between PCH2a and control lines of respective differentiation.

Figure 1

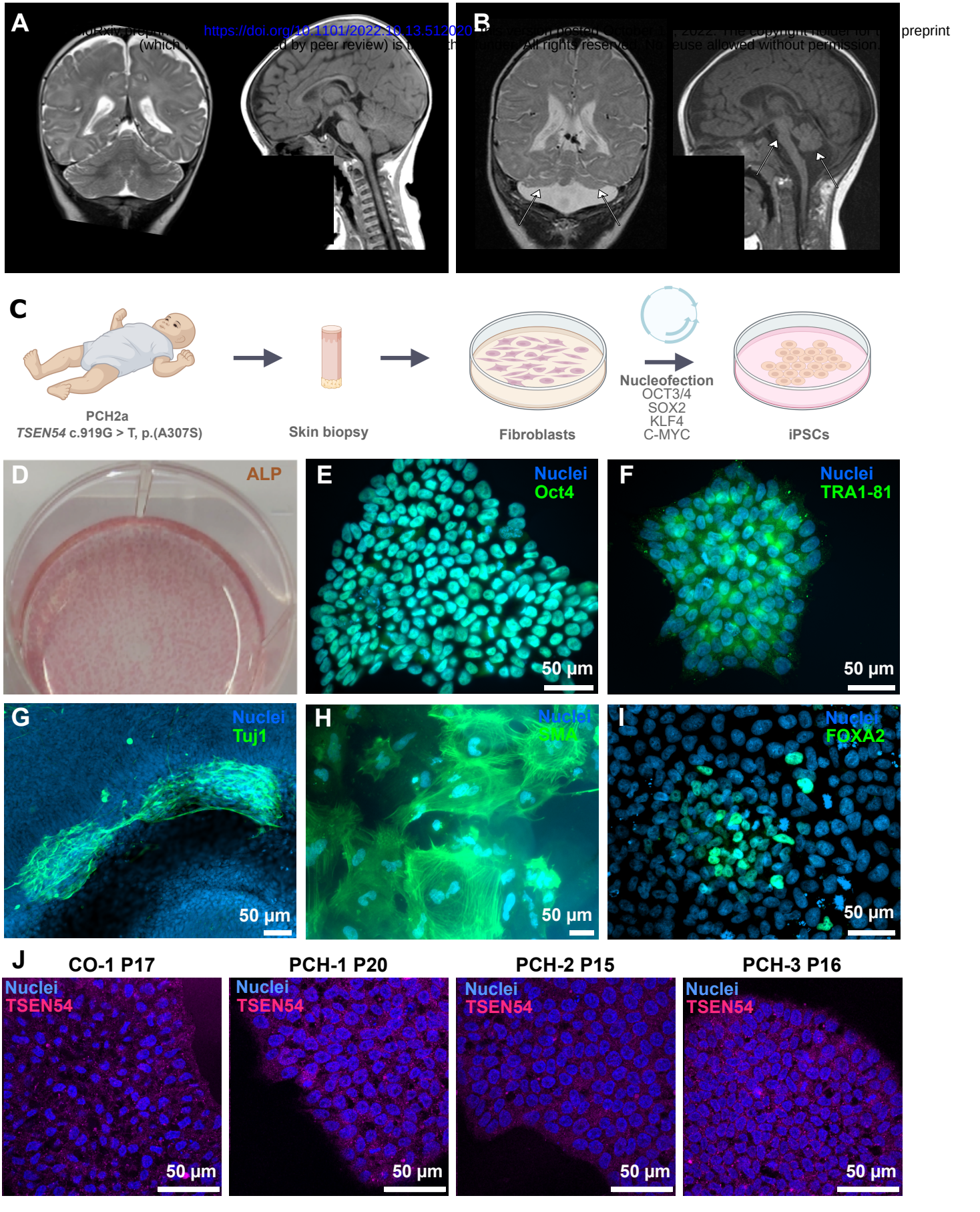

Figure 2

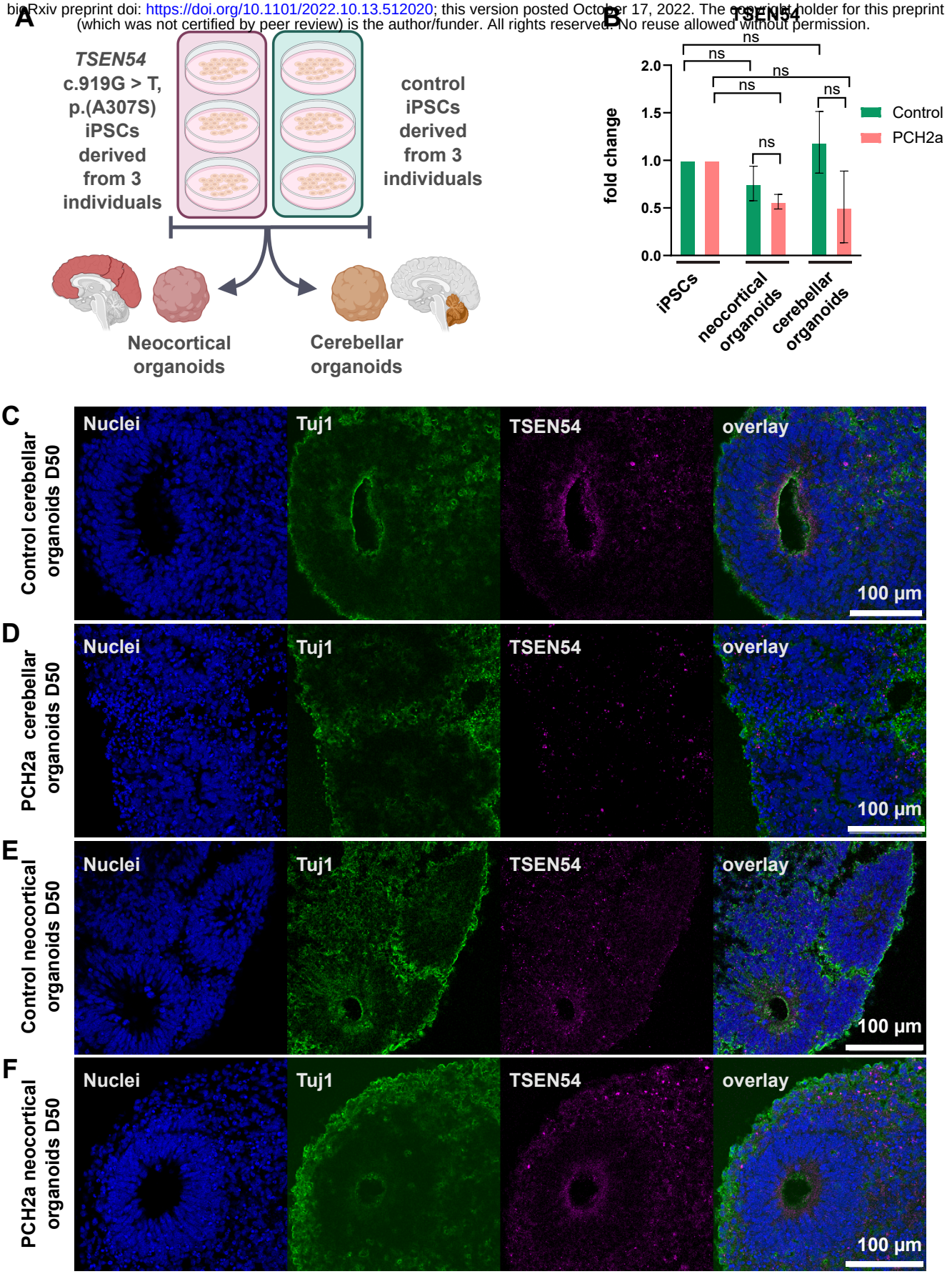

Figure 3

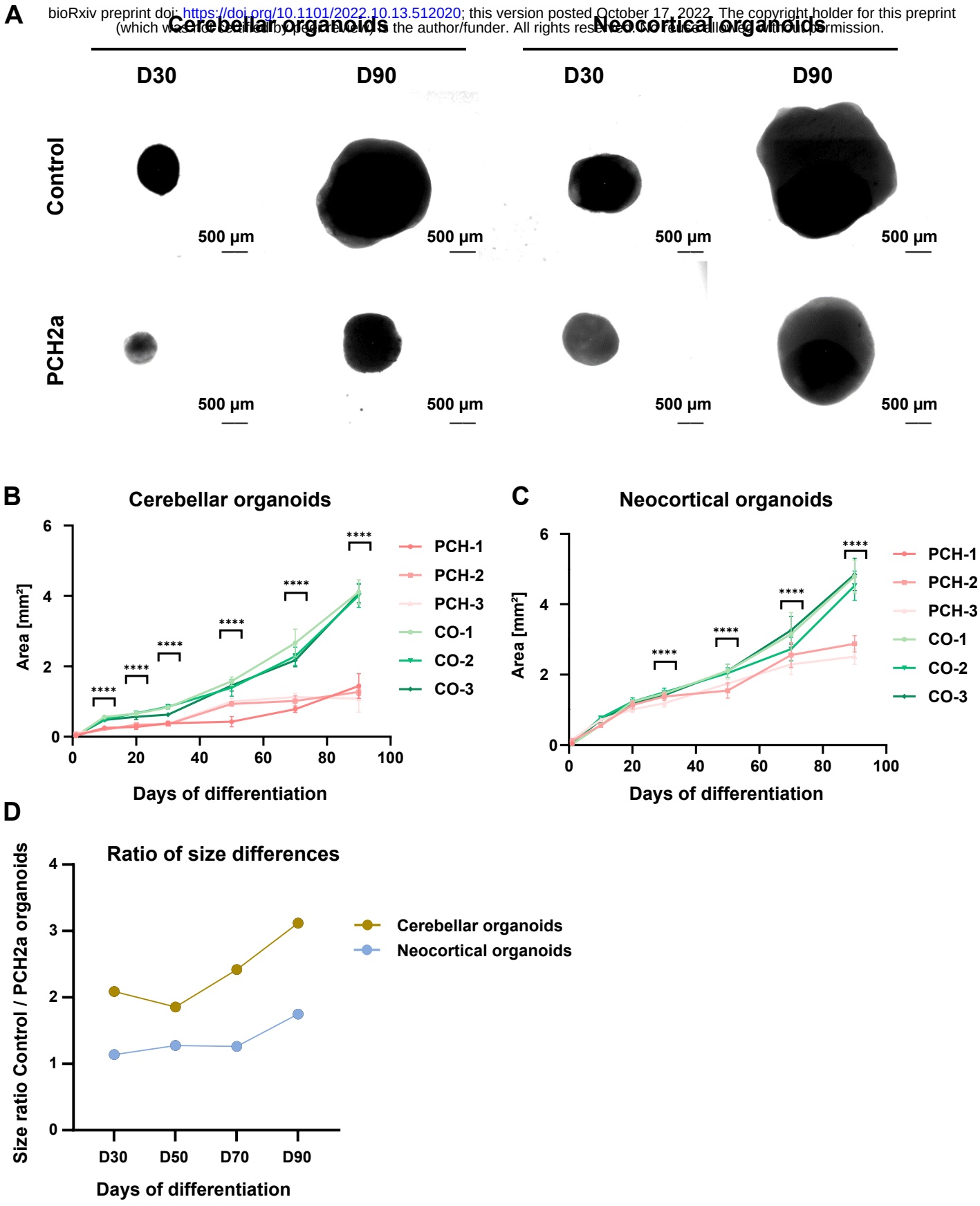

Figure 4

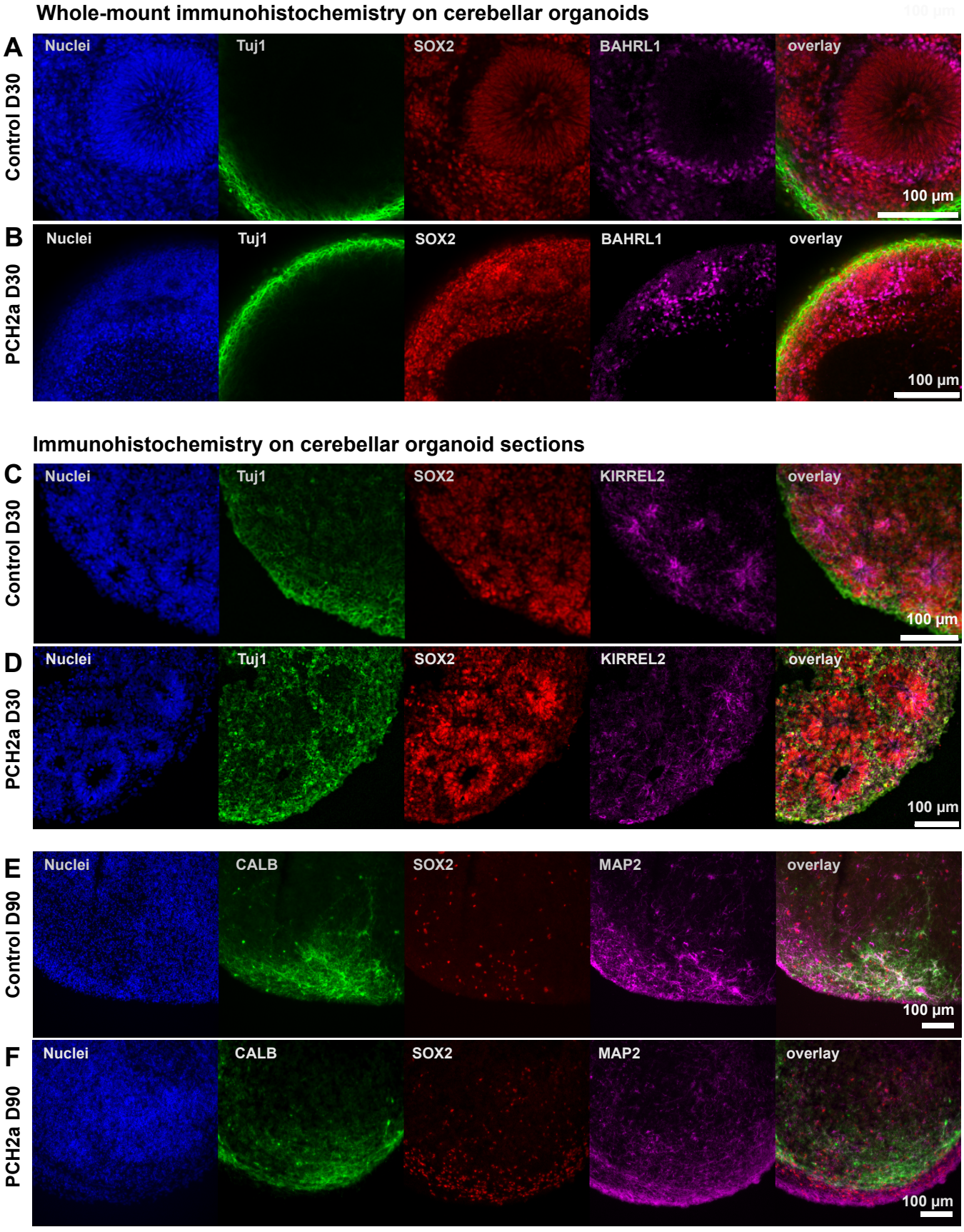

Figure 5

Immunohistochemistry on neocortical organoid sections

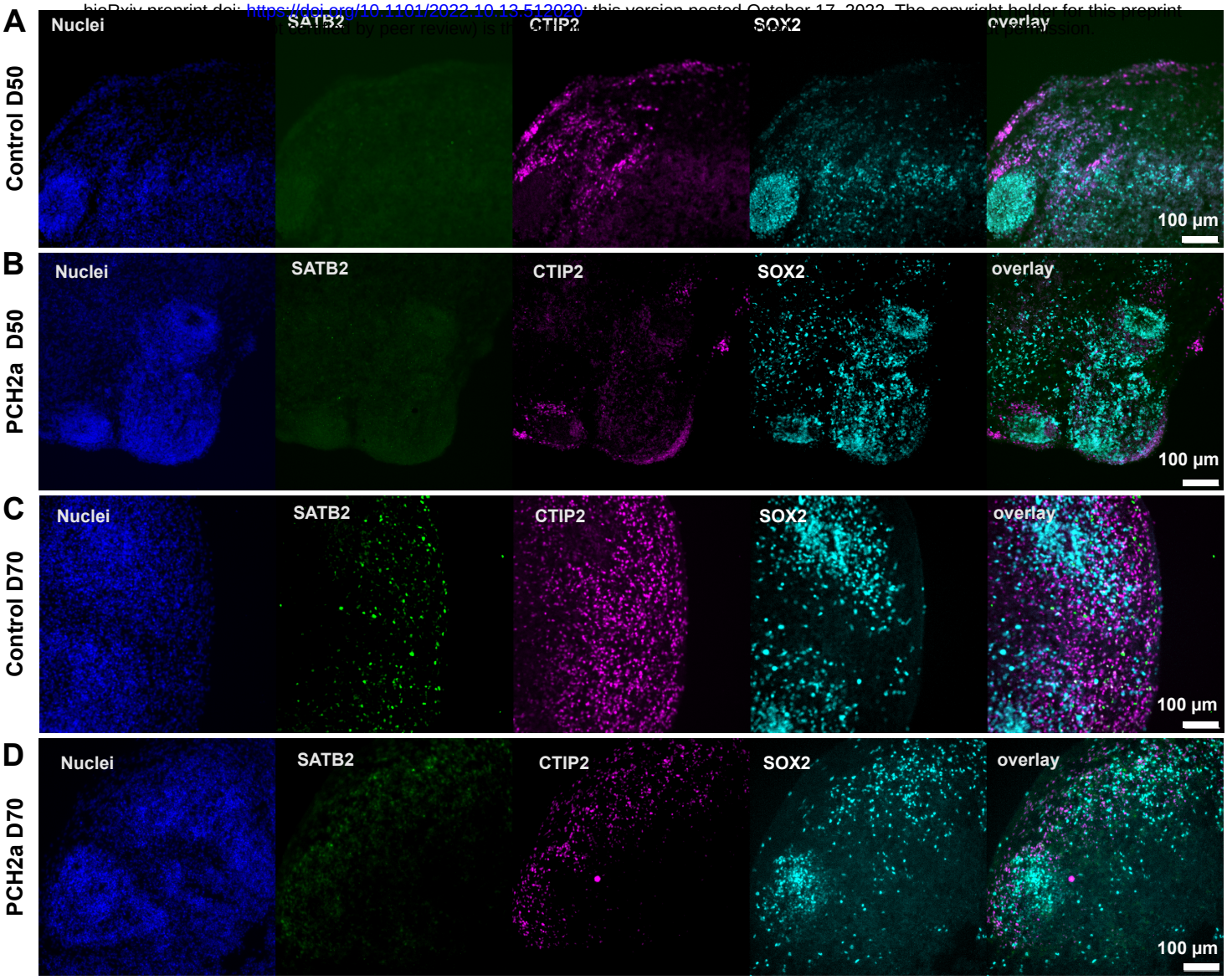

Figure 6

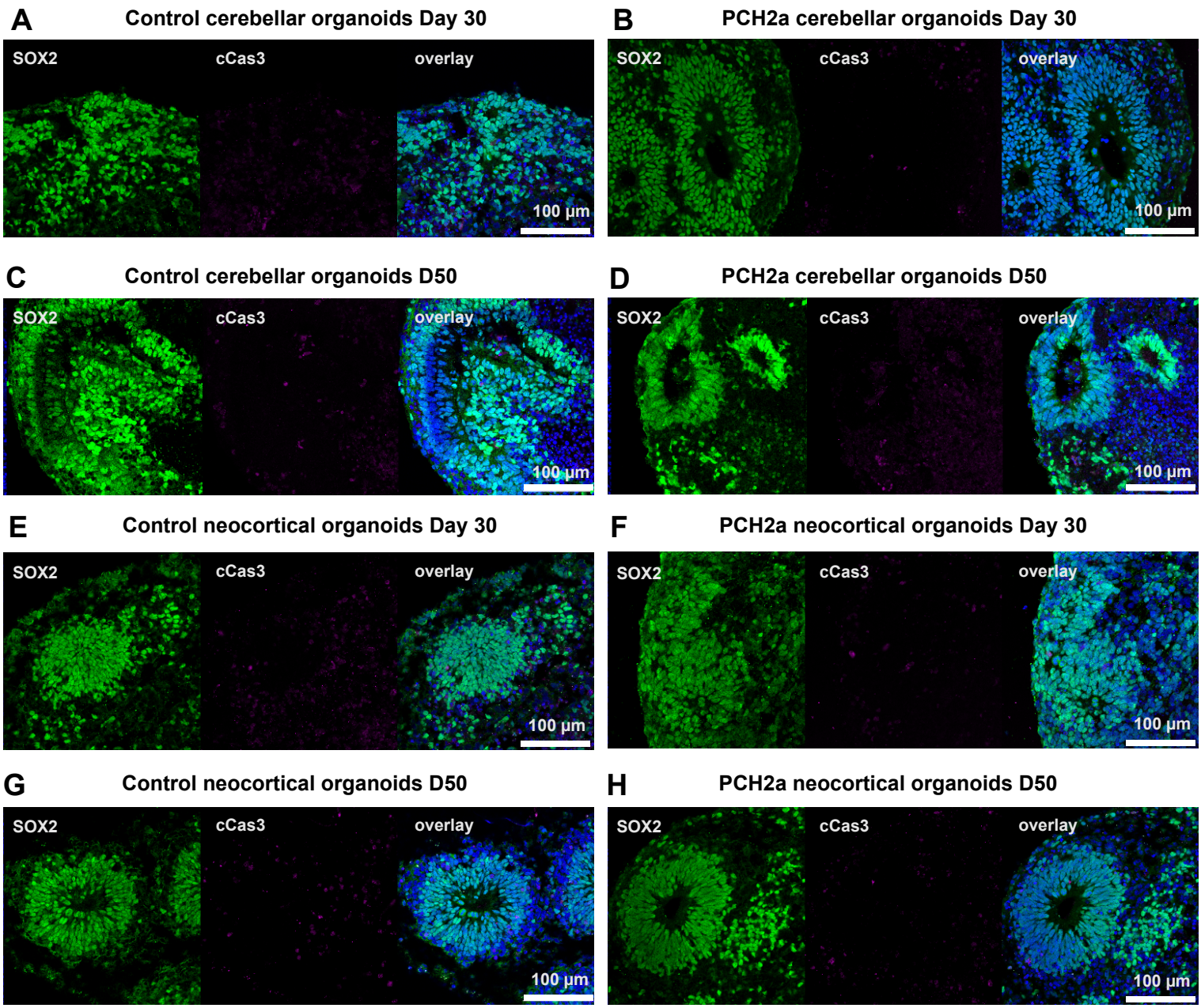

Supplementary Figure 1

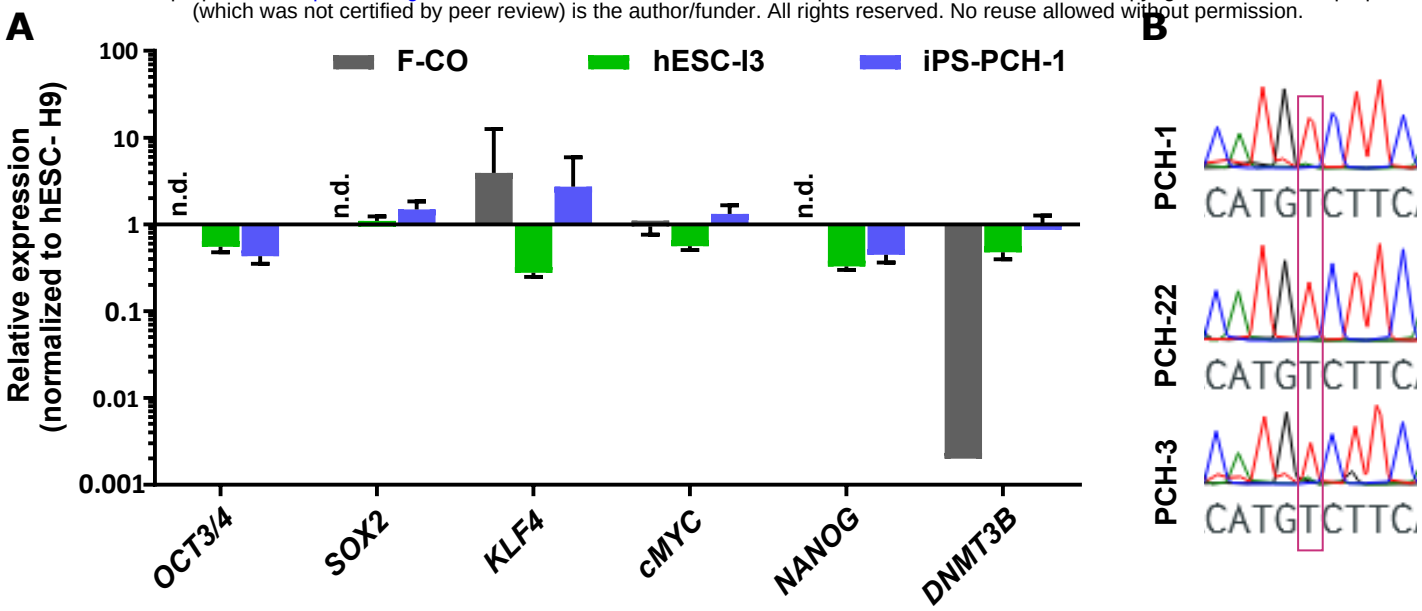

Supplementary Figure 2